

Relativistic Outflow Drives γ -Ray Emission in 3C 345

Frank K. Schinzel^{(1)*}, Andrei P. Lobanov⁽¹⁾, Gregory B. Taylor^(2,4), Svetlana G. Jorstad^(3,5), Alan P. Marscher⁽³⁾, and J. Anton Zensus⁽¹⁾

¹ Max-Planck-Institut für Radioastronomie, Auf dem Hügel 69, 53121 Bonn, Germany

² Department of Physics and Astronomy, University of New Mexico, Albuquerque NM, 87131, USA

³ Institute for Astrophysical Research, Boston University, Boston, MA 02215, USA

⁴ also an adjunct astronomer at the National Radio Astronomy Observatory

⁵ St.Petersburg State University, St.Petersburg, Russia

accepted by A&A: 29/10/2011

ABSTRACT

Aims. 3C 345 was recently identified as a γ -ray emitter, based on the first 20 months of *Fermi*-LAT data and optical monitoring. In this paper, a connection between the γ -ray and optical variability of 3C 345 and properties of its parsec-scale radio emission is investigated.

Methods. The *Fermi*-LAT data of 3C 345, covering an energy range of 0.1–300 GeV, were combined with 32 Very Long Baseline Array observations of the object made at 43.2 GHz in the period of January 2008 – March 2010.

Results. The VLBA data reveal morphology and kinematics of the flow on scales of up to ≈ 5 milliarcseconds (deprojected linear distances of 380 parsecs). The brightness temperature, $T_b(r)$, measured along the jet first decreases with distance $\propto r^{-(0.95 \pm 0.69)}$ and later exhibits a break at ≈ 0.3 milliarcseconds (mas), with $T_b(r) \propto r^{-(4.11 \pm 0.85)}$ at larger separations. Variations of the γ -ray, optical and parsec-scale radio emission show a similar long-term trend persistent during the entire VLBA monitoring period. The γ -ray and optical variations on shorter time scales are related to structural changes in the jet on scales of ≈ 0.3 mas (≈ 23 parsecs, deprojected), with the γ -ray and optical flares possibly related to the evolution of four distinct superluminal components identified in the flow.

Conclusions. The observations indicate that both the quiescent and flaring components of the γ -ray emission are produced in a region of the jet of ~ 23 pc in extent. This region may mark the Compton-loss dominated zone of the flow and its large extent may favor the synchrotron self-Compton mechanism for γ -ray production in the relativistic jet of the quasar 3C 345.

Key words. Radio continuum: galaxies - Gamma rays: galaxies - Galaxies:active - Galaxies:jets - Galaxies: nuclei - Galaxies: individual: 3C 345

1. Introduction

Observations of high-energy emission (keV – TeV range) provide important insights into the physical properties of Active Galactic Nuclei (AGN), in particular for the subgroup of quasars. However, high energy production scenarios are still heavily debated with many possibilities discussed (e.g., Böttcher et al. 2009; Dermer et al. 2009; Błażejowski et al. 2004). Most of these physical models depend on the emission site, mainly its distance to the central engine. A connection between cm-/mm-radio and high energy emission of quasars was already suggested by Valtaoja & Terasranta (1996), Jorstad et al. (2001) and references therein. To investigate this connection, variability of AGN are studied in coordinated multi-wavelength observation campaigns covering radio to γ -ray wavelengths. Their results, especially on archetypal sources, are essential for the physical understanding of the emission processes in AGN up to the highest energies (cf. Longair 2011). These observations, in particular simultaneous high-resolution very long baseline interferometry (VLBI) observations at mm-wavelengths, provide new limits on the parameter space of proposed emission models, placing constraints on size, energetics and locations of emission regions.

The archetypal quasar 3C 345 is one of the best studied “superluminal” radio sources, with its parsec-scale radio

emission monitored over the past 30 years, in particular by VLBI (e.g.: Biretta et al. 1986; Baath et al. 1992; Lobanov 1996; Zensus et al. 1995; Ros et al. 2000; Klare 2004; Jorstad et al. 2007). Based on previous observations, spectral index and turnover frequency distributions were obtained (Lobanov 1996, 1998a; Ros et al. 2000), the spectral evolution of the jet was studied (Lobanov & Zensus 1999), properties of radio and X-ray emission were related (Unwin et al. 1997; Lobanov & Roland 2005), the dynamics of the central region was investigated (Lobanov & Roland 2005) and opacity in the nuclear region was used to determine the physical properties and matter composition of the compact jet (Lobanov 1998b; Hirokani 2005). Quasi-periodic variations of emission have been detected in the optical (Babadzhanyants & Belokon 1984; Kidger & Takalo 1990) and radio (Aller et al. 1996; Terasranta et al. 1998; Lobanov & Zensus 1999) regimes with a possible periodicity of 3.5–4.5 years and major flares occurring every 8–10 years. A new cycle of such enhanced nuclear activity began in early 2008 (Larionov et al. 2009).

The identification of 3C 345 as a γ -ray source was unclear during the EGRET-era (1991–2000; Thompson et al. 1993) with a possible weak detection between April and May, 1996 (Casandjian & Grenier 2008). The γ -ray emission detected by the Large Area Telescope (LAT), on board the *Fermi* satellite, in the vicinity of 3C 345 was initially associated with another quasar in the region, B3 1640+396 with low confidence, based on the 3-month data (August – October, 2008) collected

* Member of the International Max Planck Research School (IMPRS) for Astronomy and Astrophysics at the Universities of Bonn and Cologne.

(Abdo et al. 2009). However, with 20 months (August 2008 – April 2010) of LAT monitoring data, 3C 345 was identified as a γ -ray source at GeV energies, based on multi-wavelength counterpart localizations and correlated variability (Schinzel et al. 2011).

This paper presents results from a coordinated observational campaign targeting 3C 345 and combining the 20-month *Fermi*-LAT γ -ray monitoring data (Schinzel et al. 2011) with monthly VLBI observations made at 43.2 GHz (7 mm wavelength) at the VLBA¹. Section 2 discusses the observations and data reduction methods applied to obtain calibrated datasets for further analysis. It discusses in particular the criteria that were developed in order to determine the statistical significance of the 2D-Gaussian models (modelfits) applied to the observed radio brightness distribution. In Section 3 we present kinematics of the pc-scale radio jet and flux density evolution, and a possible connection with the high energy γ -ray emission. Section 4 discusses the findings of this paper and in Section 5 conclusions are made from the results presented here.

Throughout this paper a flat Λ CDM cosmology is assumed, with $H_0 = 71 \text{ km s}^{-1} \text{ Mpc}^{-1}$ and $\Omega_M = 0.27$. At the redshift $z = 0.593$ (Marziani et al. 1996) of 3C 345 this relates to a luminosity distance $D_L = 3.47 \text{ Gpc}$, a linear scale of 6.64 pc mas^{-1} and a proper motion scale of 1 mas year^{-1} corresponding to 34.5 c .

2. Observations & Data Analysis

2.1. *Fermi*-LAT

The *Fermi*-LAT (Atwood et al. 2009) is a pair conversion telescope designed to cover the energy band from 20 MeV to greater than 300 GeV. It is the product of an international collaboration between NASA and DOE in the U.S. and many scientific institutions across France, Italy, Japan, and Sweden.

The γ -ray emission of 3C 345 was identified based on correlations found between the optical variability and major γ -ray events observed by *Fermi* LAT between August 2008 and April 2010. The γ -ray counterpart of 3C 345 was localized to R.A. $16^{\text{h}}43^{\text{m}}0.24^{\text{s}}$, Dec. $+39^{\circ}48'22.7''$ (Schinzel et al. 2011). For this paper a light curve for which the γ -ray monitoring data was split into regular time intervals, each integrating over periods of 7 days and an energy range of 0.1–300 GeV, was obtained in the fashion described in Schinzel et al. (2011). The position of the γ -ray counterpart was fixed to the radio localization of 3C 345. For the spectral shape of the γ -ray emission of 3C 345 a power-law was used with the spectral index fixed to its 20 month average value of $\Gamma = 2.45^2$. The particular time binning of 7 days in this case provides the best trade-off between time resolution and signal to noise. This yielded a light curve with 81 significant detections and five 2σ upper limit time intervals (JD 2454756, 2454826, 2454903, 2454945, 2455155), in total this covers a time period of 602 days (20 months). In order to homogenize the light curve, 2σ upper limits were used as values with their error estimate for that interval replaced with half the difference between that upper limit and its value determined through the unbinned spectral likelihood analysis. This method was applied for the calculation of the variability index in Schinzel et al. (2011) and Abdo et al. (2010).

¹ Very Long Baseline Array of the National Radio Astronomy Observatory, Socorro, USA

² The photon spectral index Γ is defined as $N(E) \propto E^{-\Gamma}$, where $N(E)$ is the γ -ray photon flux as a function of energy E .

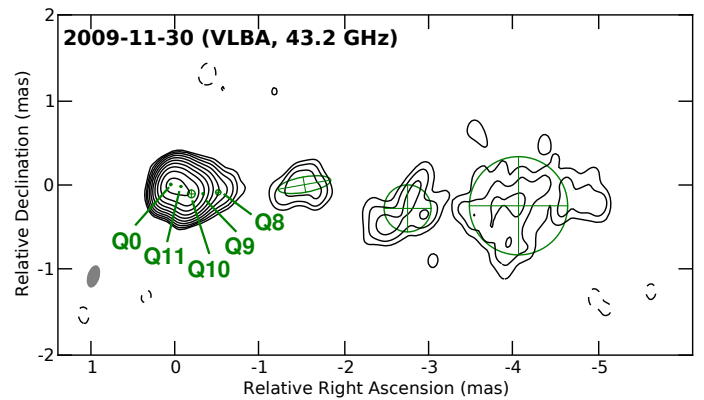


Fig. 1. VLBA image of the total brightness distribution of 3C 345 at 43.2 GHz made from observations on Nov. 30, 2009. Open crossed circles show the FWHM of eight Gaussian components applied to fit the structure observed. The shaded ellipse, in the lower left corner, represents the FWHM of the restoring beam. The image peak flux density is 2.1 Jy beam^{-1} and the RMS noise is 1 mJy beam^{-1} . The contour levels are $(-0.15, 0.15, 0.3, 0.6, 1.2, 2.4, 4.8, 9.6, 19, 38, 77) \%$ of the peak flux density. Here the nuclear region is modeled by two circular Gaussian components (Q0, Q11) identified as the best representation of the observed brightness distribution.

2.2. Very Long Baseline Array (VLBA)

Following the onset of a new period of flaring activity in 2008, a dedicated monthly monitoring campaign was initiated, using the VLBA to monitor the radio emission of 3C 345 at 43.2, 23.8, and 15.4 GHz (VLBA project codes: BS193, BS194). In this paper only the 43.2 GHz observations are discussed, while the analysis of 15.4 and 23.8 GHz data is continued. The observations were made with a bandwidth of 32 MHz (total recording bit rate 256 Mbits s^{-1}). A total of 12 VLBA observations were completed, with about 4.5 hours at 43.2 GHz spent on 3C 345 during each observation. Scans on 3C 345 were interleaved with observations of J1310+3233 (amplitude check, EVPA calibrator), J1407+2827 (D-term calibrator), and 3C 279 (amplitude check, EVPA calibrator). The VLBA data were correlated at the NRAO VLBA hardware correlator and starting from December 2009 the new VLBA-DiFX correlator was employed. Analysis was done with NRAO’s Astronomical Image Processing System (AIPS) and Caltech’s Difmap (Shepherd et al. 1995) software for imaging and modeling. Corrections were applied for the parallactic angle and for Earth’s orientation parameters used by the VLBA correlator. Fringe fitting was used to calibrate the observations for group delay and phase rate. A summary of all the observations is presented in Table 1. Here, the data from the 12 epochs of this dedicated monitoring campaign are presented, combined with 20 VLBA observations from the blazar monitoring program of Marscher et al. (VLBA project codes BM256, S1136) available online³. The combined data (see Table 1) cover a period from January 2008 to March 2010, with observations spaced roughly at monthly intervals or shorter.

The brightness distribution of the radio emission was model-fitted by multiple Gaussian components providing positions, flux densities and sizes of distinct emitting regions in the jet. Fig. 1 illustrates the observed radio structure and the Gaussian modelfit representation. In the following, we interpret the eastern-most Gaussian modelfit component obtained from

³ <http://www.bu.edu/blazars/VLBAproject.html>

Table 1. Summary of VLBA Observations.

Date	S_{tot} [Jy]	D	Beam (bpa) [mas]×[mas] (°)	Ref.
2008-01-17	1.90	2300	0.31×0.19 (-27.2)	1
2008-02-29	2.02	1600	0.37×0.21 (-29.1)	1
2008-06-12	2.44	2100	0.38×0.16 (-28.2)	1
2008-07-06	2.23	800	0.33×0.15 (-16.6)	1
2008-08-16	3.78	2700	0.41×0.19 (-30.2)	1
2008-09-10	3.67	4300	0.37×0.19 (-32.5)	1
2008-11-16	4.43	300	0.37×0.33 (-1.49)	1
2008-12-21 [†]	2.91	5500	0.39×0.17 (-16.9)	1
2009-01-24	5.04	8900	0.31×0.17 (-20.5)	1
2009-02-19 [†]	3.55	2200	0.37×0.20 (-19.0)	2
2009-02-22	4.63	8800	0.35×0.15 (-19.1)	1
2009-03-16	6.01	2400	0.43×0.30 (9.31)	2
2009-04-01	5.67	8000	0.33×0.16 (-18.7)	1
2009-04-21	5.78	2600	0.33×0.22 (-16.7)	2
2009-05-27	7.00	3500	0.33×0.18 (-15.2)	2
2009-05-30	8.65	6900	0.32×0.16 (-19.8)	1
2009-06-21	5.04	6500	0.28×0.16 (-10.9)	1
2009-06-29	6.43	2600	0.29×0.16 (-11.6)	2
2009-07-27	7.63	2900	0.38×0.16 (-30.8)	2
2009-08-16	5.80	4300	0.30×0.16 (-20.4)	1
2009-08-26	6.58	2000	0.32×0.17 (-24.8)	2
2009-09-16	6.75	4600	0.35×0.19 (18.3)	1
2009-10-01	6.67	2300	0.22×0.18 (-21.6)	2
2009-10-16	6.80	4800	0.41×0.17 (-30.5)	1
2009-11-07	6.38	1400	0.32×0.16 (-15.3)	2
2009-11-28	5.31	4900	0.28×0.16 (-24.6)	1
2009-11-30	5.53	2000	0.29×0.16 (-16.9)	2
2009-12-28	4.95	2400	0.31×0.16 (-8.14)	2
2010-01-10	4.25	2400	0.33×0.20 (-8.75)	1
2010-02-11	5.57	2100	0.27×0.15 (-17.0)	1
2010-02-15	5.11	1300	0.31×0.20 (-6.37)	2
2010-03-06	5.38	3300	0.39×0.28 (-12.1)	1

Notes: S_{tot} – total flux density recovered in VLBA image;

D – dynamic range measured as a ratio of the image peak flux density to the RMS noise;

Beam (bpa) – beam size, major axis vs minor axis with position angle of ellipse in parentheses;

References: 1 – blazar monitoring Marscher et al. (VLBA project codes BM256, S1136); 2 – dedicated monitoring (VLBA project codes BS193, BS194).

[†] – not used for the flux density analysis due to gain calibration problems and bad weather conditions on some of the VLBA antennas.

the VLBI map, hereafter labeled as Q0 (see Fig. 1), as the base (or “core”) of the radio jet at 43.2 GHz. The remaining features can signify perturbations or shocks developing in the jet. Locations and proper motions of these jet features are then determined with respect to Q0.

To find the best description of the observed brightness distribution, compact emission in the nuclear region (≤ 0.15 mas from Q0) was modeled using four different approaches: 1) single circular Gaussian, 2) single elliptical Gaussian, 3) two circular Gaussians, 4) three circular Gaussians. In the following discussion, these modelfitting approaches are designated 1C, 1E, 2C and 3C, respectively.

The criterion for significant improvement between two modelfits was developed using a ratio of reduced χ^2 parameters

$$\frac{\chi_1^2}{\chi_2^2} \geq \frac{x_{0.68;2}}{x_{0.68;1}},$$

$$(1) \quad \text{if } (r > 0) : \sigma_\Phi = \arctan\left(\frac{\sigma_r}{r} \cdot \frac{180}{\pi}\right).$$

where the subscripts refer to the two modelfits compared. The order is defined by the number of degrees of freedom n of the individual modelfits with the condition $n_1 < n_2$. The parameter $x_{0.68}$ is obtained by solving the equation of the cumulative distribution function (CDF) of the χ^2 distribution,

$$0.68 = \frac{1}{\Gamma\left(\frac{n}{2}\right)} \gamma\left(\frac{n}{2}, \frac{x_{0.68}}{2}\right), \quad (2)$$

where Γ denotes Euler’s Gamma function and γ represents the lower incomplete Gamma function. The number of degrees of freedom, n , depends on the number of modelfit parameters, since $\chi_\alpha^2 = \chi_{\min}^2 + x_\alpha(n, \alpha)$, with α describing the significance level ($\alpha = 0.68$, in our case). The proof and application of this property are discussed in Avni (1976).

Fig. 2 compares the χ^2 parameters of each modelfit, normalized to the χ^2 values of the 1C (top panel), 1E (middle panel) and 2C (bottom panel). The horizontal lines in the plots represent the upper thresholds for significant improvement over the labeled Gaussian model. The 1C models compared to the 1E and 2C models have the respective threshold values of 0.77 and 0.82. 1E models compared to 2C models have a threshold value of 0.91, and 2C compared to 3C models needs to have an improvement of 0.86 or less. For some of the observations, the representation of the nuclear region by 1E is comparable to 2C. However, in order to form a consistent dataset, we adopt the representation by 2C providing the optimal ratio of χ^2 to the number of model parameters for all epochs.

The errors of the obtained modelfit parameters were estimated from the image plane, following analytical approximations introduced by Fomalont (1999) and Lobanov (2005) with modifications to account for the strong side-lobe case inherent to VLBI observations. For each component in the model, the root-mean-square (RMS) noise (σ_p) was determined measuring around its position in the residual image. Then the respective component was removed from the Gaussian model and the modified model was subtracted from the data, yielding an image that contained only the contribution from the component investigated. The flux density (S_p) at the peak position of the Gaussian was taken. Further input values were, observation beam size ($b = \sqrt{b_{\text{maj}} \cdot b_{\text{min}}}$), component total flux density (S_t), component distance (r), position angle (Φ), and size (d). The errors for the model fit parameters were calculated in the following way:

$$SNR = \frac{S_p}{\sigma_p} \quad (SNR > 1) \quad (3)$$

$$\sigma_t = \left(\sigma_p \cdot \sqrt{1 + SNR}\right) \sqrt{1 + \left(\frac{S_t^2}{S_p^2}\right)} \quad (4)$$

$$d_{\text{lim}} = \frac{4}{\pi} \cdot \sqrt{\pi \ln(2.0) \cdot b \cdot \ln\left(\frac{SNR}{SNR - 1}\right)}; \quad (5)$$

$$\text{if } (d_{\text{lim}} > d) \quad \text{else} \quad (d_{\text{lim}} = d) \quad (6)$$

$$\sigma_d = \frac{\sigma_p \cdot d_{\text{lim}}}{S_p} \quad (7)$$

$$\sigma_r = 0.5 \cdot \sigma_d \quad (8)$$

$$(1) \quad \text{if } (r > 0) : \sigma_\Phi = \arctan\left(\frac{\sigma_r}{r} \cdot \frac{180}{\pi}\right). \quad (9)$$

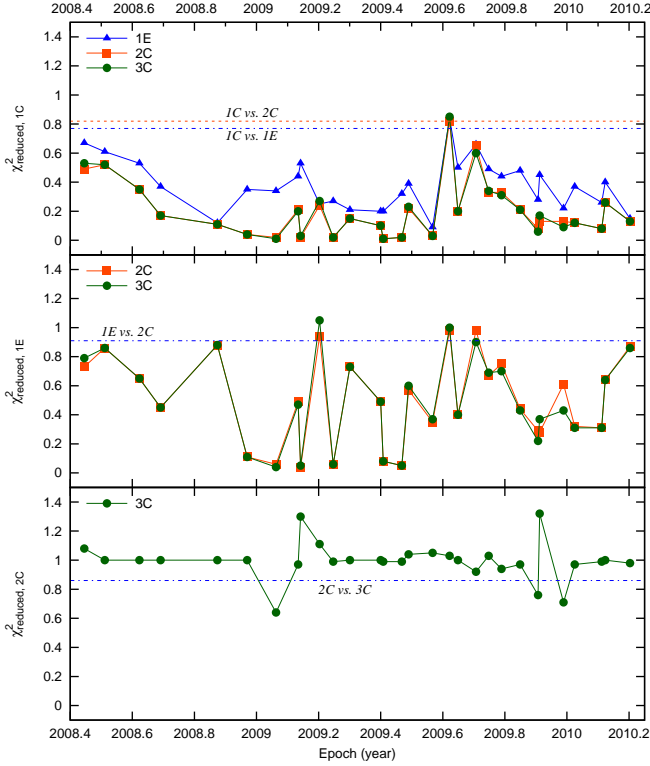


Fig. 2. Reduced χ^2 parameters of the modelfit representations of the core region. The top panel shows the resulting χ^2_{reduced} values of 1E, 2C and 3C Gaussian models normalized to the value of the 1C Gaussian representation. The two horizontal lines mark the limit below which, for the corresponding model, a significant improvement (68% confidence) over 1C is given (0.77, 0.82). Similarly the middle panel shows the χ^2_{reduced} values for 2C and 3C normalized to that of 1E. The horizontal line marks the significant improvement level compared to 2C (0.91). The bottom panel normalizes the χ^2 values to that of 2C. The dashed line plots the significant improvement limit for 3C (0.86).

These error estimates only reflect the statistical image errors and are assumed uncorrelated. No additional systematic errors were taken into account, such as errors of the amplitude calibration that could add an additional uncertainty to the determined flux density values.

3. Results

3.1. Evolution of the radio emission in the nuclear region

Comparisons of the component positions, flux densities and sizes determined from the Gaussian modelfits revealed a new moving emission region, labeled Q9, first detected in the VLBA image from June 16, 2008, followed by detections of another new component on January 24, 2009 (Q10), a third one on July 27, 2009 (Q11), and a fourth on November 28, 2009 (Q12). In the following, components Q9, Q10, Q11 and Q12 (Fig. 1) observed within a distance of 0.5 mas from the core Q0 are referred to as the “jet”.

3.1.1. Kinematics

We determine the kinematics of individual features from their relative positional offsets with respect to Q0. The temporal evo-

lution of the measured offsets is plotted in Fig. 3. The component Q8, which was first observed in 2007, is also included for the purpose of comparison.

The motions in the jet of 3C 345 are investigated using the R.A., Dec. (x , y) positions of a jet component relative to the core component (Q0) over the observed periods, fitting them separately using polynomials of different order (cf. Zensus et al. 1995) and applying the following procedure:

1. The first order polynomial is fitted to the trajectory using the nonlinear least-squares Marquardt-Levenberg algorithm (as implemented by *gnuplot*).
2. The second order polynomial is fitted to the trajectory and if the improvement of the reduced χ^2 satisfies the criterion described in Section 2.2, the fit is accepted.
3. The order of the fit polynomial is increased until no improvement according to the χ^2 statistics is achieved.

Using this approach, we find that it is sufficient to represent the trajectories of components Q8, Q11 and Q12 by linear fits in both the x and y directions. In the case of components Q9 and Q10, a second order polynomial represents the best fit to the observed data in the x direction, implying apparent acceleration. In the y direction a linear fit is sufficient. The resulting fitted radial separations, $r(t) = \sqrt{x(t)^2 + y(t)^2}$, are drawn in Fig. 3. For each component, the fits yield average proper motion and mean angular speed $\langle\mu\rangle$ and the average direction of motion $\langle\Phi\rangle$. The kinematic properties thus derived for the jet components indicate that Q9 and Q10 underwent a clear phase of apparent acceleration over a period of 1.5 years and over a distance of ~ 0.3 mas (2 pc). No statistically significant acceleration was observed for Q8, Q11 and Q12. The observed values for $\langle\mu\rangle$ are in the range of 0.25 – 0.42 mas year $^{-1}$ and for $\langle\Phi\rangle$ in the range of -96 to -120° , also see Table 2. Jorstad et al. (2005) previously reported apparent jet component speeds of 0.29 – 0.69 mas year $^{-1}$ and a jet position angle of -66 – -95° . Using $\langle\mu\rangle$, the average apparent speed $\bar{\beta}_{\text{app}}$ and the speed in the source frame (deprojected) $\bar{\beta}$ are derived through,

$$\bar{\beta}_{\text{app}} = \langle\mu\rangle \frac{D_L}{(1+z)} \quad (10)$$

and

$$\bar{\beta} = \frac{\bar{\beta}_{\text{app}}}{\bar{\beta}_{\text{app}} \cos \Theta + \sin \Theta}, \quad (11)$$

where D_L is the luminosity distance, z is the redshift and Θ is the jet angle to the line of sight (viewing angle).

As a final step the physical parameters, Doppler factor δ , Lorentz factor Γ and viewing angle Θ of each jet component are derived. For the following calculations, we assume that the jet emission is dominated by radiative losses (see e.g., Jorstad et al. 2005) and consist of optically thin shocked gas, $\alpha = -0.7$ (i.e. $S_\nu \propto R^{-1.633} \cdot \nu^{+\alpha}$, where R is the size of the emitting region in the rest-frame of the jet and ν the frequency in the observer’s frame, Marscher & Gear 1985). The variability Doppler factor is then derived as,

$$\delta_{\text{var}} = \frac{d_{\text{eff}} D_L}{c \Delta t_{\text{var}} (1+z)}, \quad (12)$$

where D_L is the luminosity distance and d_{eff} is the effective angular size of a spherical region (i.e. the measured FWHM of the component multiplied by a factor of 1.8; cf. Pearson 1999). The flux variability time scale is defined as $\Delta t_{\text{var}} = dt / \ln(S_1/S_2)$.

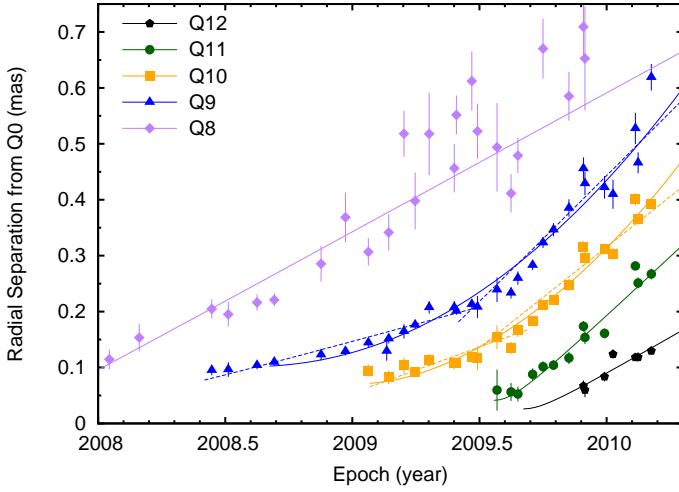


Fig. 3. Evolution of the radial separations from the core of components Q12, Q11, Q10, Q9 and Q8. Q12-Q9 are related to the radio variability since 2008, Q8 is related to a previous radio flare observed in 2007. The lines are the results of polynomial fits to $x(t)$ and $y(t)$ directions separately. The dashed lines are the results of linear fits to $x(t)$ and $y(t)$ to determine ejection epochs and speeds for the two cases discussed in Section 3.1.2.

The value of S_1 is the measured maximum component flux density, while S_2 represents the minimum component flux density selected at the time of maximum absolute value of the time derivative of the flux density. It is then possible to calculate bulk Lorentz factors by combining the derived δ_{var} with β_{app} ,

$$\Gamma_{\text{var}} = \frac{\beta_{\text{app}}^2 + \delta_{\text{var}}^2 + 1}{2\delta_{\text{var}}}. \quad (13)$$

Combining the derived values for all components, a mean Lorentz factor of 12.5 and a mean Doppler factor of 14.4 are obtained (see Table 2).

An upper limit for the viewing angle Θ can immediately be determined using the average apparent component speed β_{app} and the relation $\delta_{\text{min}} = \sqrt{1 + \beta_{\text{app}}^2}$. This combined with the equation

$$\Theta = \arctan \frac{2\beta_{\text{app}}}{\beta_{\text{app}}^2 + \delta^2 - 1}, \quad (14)$$

yields $\Theta \leq 5.2^\circ$. Using the variability time scale argument and the derived values of δ_{var} from above, the values Θ_{var} for each component are obtained, which together have a mean Θ_{var} of $4.7^{+0.65}_{-0.51}$, consistent with our upper limit. Pushkarev et al. (2009) obtained a similar value of $\Theta = 5.1^\circ$, which was determined by combining the component speeds at 15 GHz and variability Doppler factors derived from single-dish observations at 37 GHz. Earlier, Jorstad et al. (2005) obtained a smaller viewing angle of $2.7^\circ \pm 0.9^\circ$ using VLBI data at 43.2 GHz alone. In the following discussion, we adopt $\Theta = 5^\circ$.

3.1.2. Ejection Epochs

With the kinematics determined in Section 3.1.1, it is possible to estimate the time at which a moving jet feature passes the VLBI core at 43 GHz. These passages are referred to as ejection epochs. The ejection epoch also marks the time at which a new jet feature begins to contribute to the observed radio emission.

As a first approach to determine the ejection epochs, we assume that the jet is optically thin all the way to the core and the features already travel at the observed average speed while passing through the VLBI core. Under these assumptions the ejection epoch is determined by back tracing the fitted linear trajectories. The resulting ejection epochs for all features are listed in Table 2, as well. This approach provides reasonable estimates of the ejection epochs for non-accelerating features, while for the apparently accelerating components Q9 and Q10 a different approach is required.

Looking at the radial separations of Q9 and Q10 in Fig. 3, the acceleration is most evident for the time before 2009.6. An upper limit on the ejection epoch can be determined using a linear fit to the data points after 2009.5 for Q9 and 2009.4 for Q10 (τ_{upper} in Table 2). Similarly, lower limits, τ_{lower} , on the ejection epochs of Q9 and Q10 are obtained by considering only data points before 2009.5 and 2009.4 respectively.

3.1.3. Jet Intensity Gradient

In flat spectrum radio quasars (FSRQs), such as 3C 345, the component flux decay is commonly driven by radiative losses (Lobanov & Zensus 1999; Jorstad et al. 2005), which was assumed in Section 3.1.1 without further justification. To test this, the maximum component brightness temperature needs to be calculated as a measure for the emission intensity of each component, using:

$$T_b = 1.22 \cdot 10^{12} \cdot \frac{S_{\text{comp}} \cdot (1+z)}{d_{\text{comp}}^2 \cdot \nu^2}, \quad (15)$$

where S_{comp} is the component flux density in Jansky, z the redshift of the source, d_{comp} the FWHM size of the circular Gaussian in mas and ν the observing frequency in GHz. In Fig. 4 the brightness temperatures for components Q9, Q10 and Q11 are plotted as a function of the radial separation from the core.

In the common picture of the shock-in-jet model, a relativistic shock propagates down a conical jet, slowly expanding adiabatically albeit maintaining shock conditions. In this scenario the assumption of a power-law electron energy distribution ($N(E) dE \propto E^{-s} dE$), a power-law magnetic field evolution ($B \propto r_{\text{jet}}^{-a}$) and a constant jet opening angle with the jet transverse size proportional to the distance along the jet ($d_{\text{jet}} \propto r_{\text{jet}} \sin \Theta$) can be made. While the shock continues to travel down the jet, it undergoes three major evolutionary stages dominated by Compton, synchrotron and adiabatic energy losses (Marscher et al. 1992). From this it follows that the brightness temperature decays as a power-law, $T_{b,\text{jet}} \propto r_{\text{jet}}^{-\epsilon}$, where r_{jet} is the distance in the jet at which $T_{b,\text{jet}}$ is measured. The value of ϵ can be derived from spectral evolution of radio emission (Lobanov & Zensus 1999), assuming $T_b \propto S_{\text{comp}} / (r_{\text{jet}}^2 \nu^2)$ and the Doppler factor $\delta = \text{const.}$

For Compton (ϵ_c), synchrotron (ϵ_s) and adiabatic (ϵ_a) losses, ϵ are calculated as follows,

$$\epsilon_c = [(s+5) + a(s+1)]/8, \quad (16)$$

$$\epsilon_s = [4(s+2) + 3a(s+1)]/6 \quad (17)$$

$$\epsilon_a = [2(2s+1) + 3a(s+1)]/6 \quad (18)$$

with a typical value of $s = 2.0$ (corresponding to a synchrotron spectral index $\alpha = -0.5$; $S_\nu \propto \nu^{+\alpha}$) and $a = 1$ (dominant transverse magnetic field), $\epsilon_c = 10/8 = 1.25$, $\epsilon_s = 25/6 \approx 4.17$ and $\epsilon_a = 19/6 \approx 3.17$. For the slopes to be shallower than these derived values, acceleration resulting in increasing Doppler factors of $\delta \propto r_{\text{jet}}^b$ may be considered. For a moderate acceleration (i.e.

Table 2. Measured and derived physical parameters for radio emission regions in the inner jet ≤ 0.7 mas (4.6 pc).

Label	Q8	Q9	Q10	Q11	Q12
#	26	30	23	13	7
$\langle \mu \rangle (\beta_{\text{app}})$	0.248 ± 0.022 (8.5c)	0.277 ± 0.012 (9.5c)	0.300 ± 0.011 (10c)	0.427 ± 0.020 (15c)	0.272 ± 0.027 (9.0c)
$\langle \mu_{\text{lower}} \rangle$	-	0.1260 ± 0.0088	0.165 ± 0.016	-	-
$\langle \mu_{\text{upper}} \rangle$	-	0.458 ± 0.089	0.360 ± 0.049	-	-
$\langle \Phi \rangle$	$-100.0^\circ \pm 2.9^\circ$	$-96.3^\circ \pm 1.1^\circ$	$-114.3^\circ \pm 1.8^\circ$	$-120.5^\circ \pm 3.5^\circ$	$-117.8^\circ \pm 5.4^\circ$
$\langle \Phi_{\text{lower}} \rangle$	-	$-97.0^\circ \pm 1.0^\circ$	$-109.7^\circ \pm 3.2^\circ$	-	-
$\langle \Phi_{\text{upper}} \rangle$	-	$-96.2^\circ \pm 1.6^\circ$	$-112.3^\circ \pm 2.1^\circ$	-	-
τ_e	2007.62 ± 0.12	2006.91 ± 0.11	2009.055 ± 0.025	2009.544 ± 0.018	2009.651 ± 0.042
τ_{lower}	-	2007.834 ± 0.083	2008.674 ± 0.073	-	-
τ_{upper}	-	2009.00 ± 0.16	2009.11 ± 0.11	-	-
S_1	0.73 ± 0.12	3.44 ± 0.16	2.301 ± 0.072	1.489 ± 0.086	2.01 ± 0.11
S_2	0.257 ± 0.078	0.311 ± 0.038	0.816 ± 0.044	0.786 ± 0.057	-
d_1	0.114 ± 0.038	0.1115 ± 0.0088	0.1012 ± 0.0067	0.0620 ± 0.0094	-
d_2	0.244 ± 0.094	0.232 ± 0.036	0.170 ± 0.016	0.06 ± 0.011	-
dt	1.33	0.715	0.385	0.204	-
Δt_{var}	1.27 ± 0.42	0.297 ± 0.016	0.371 ± 0.022	0.319 ± 0.046	-
δ_{var}	5.6 ± 2.2	23.3 ± 2.2	16.9 ± 1.4	11.9 ± 2.5	-
Γ_{var}	9.8 ± 1.4	13.61 ± 0.93	11.6 ± 0.5	15.1 ± 1.0	-
Θ_{var}	$9.4^{+2.4}_{-1.9}$	$1.70^{+0.34}_{-0.23}$	$2.97^{+0.42}_{-0.32}$	$4.66^{+0.81}_{-0.69}$	-
(*)	no	yes	yes	no	no

Notes: # – number of data points;

$\langle \mu \rangle (\beta_{\text{app}})$, $\langle \mu_{\text{lower}} \rangle$, $\langle \mu_{\text{upper}} \rangle$ – average component speed in mas year⁻¹, in parentheses the apparent speed β_{app} , for Q9 and Q10 lower and upper limits of the component speeds;

$\langle \Phi \rangle$, $\langle \Phi_{\text{lower}} \rangle$, $\langle \Phi_{\text{upper}} \rangle$ – average position angle of the component motion in degree, for Q9 and Q10 lower and upper limit;

τ_e (τ_{lower} , τ_{upper}) – Ejection epoch/time of zero separation from component labeled Q0, determined through linear extrapolation using the average component speed and component position at the midpoint, $t_{\text{mid}} = 0.5 \cdot (t_{\text{max}} - t_{\text{min}})$, of the respective dataset, for Q9 and Q10 lower and upper limits;

S_1 , S_2 – maximum, minimum (at the time of maximum absolute value of the time derivative) component flux density in units of Jy;

d_1 , d_2 – circular Gaussian model fit component FWHM in units of mas at the time of S_1 , S_2 ;

dt – time between S_{max} and S_{min} in units of years;

Δt_{var} – time variability factor in units of years;

δ_{var} , Γ_{var} , Θ_{var} – derived quantities in order of the variability Doppler and Lorentz factors, and the viewing angle to the line of sight in degrees

(*) – indicator whether component was accelerating (yes) or not (no)

The asymptotic standard errors for the fits were determined statistically using an implementation of the nonlinear least-squares

Marquardt-Levenberg algorithm with the position errors as weights. Errors of the derived parameters are 68% confidence limits determined through Monte-Carlo simulations.

$b = 0.1 - 0.2$), a value $\epsilon_c \approx 0.13$ is obtained assuming $s = 2$ and with a longitudinal magnetic field ($a = 2$).

The brightness temperature gradient along the jet, shown in Fig. 4, reveals a possible broken power-law behavior of the jet intensity gradient with a break distance of ~ 0.3 mas and the two slopes $\epsilon_1 = 0.95 \pm 0.69$ and $\epsilon_2 = 4.11 \pm 0.85$. The value of ϵ_1 is consistent with ϵ_c , with the possible indication of a mild change in δ , and ϵ_2 is consistent with the derived ϵ_s . However, at the $\sim 1\sigma$ level, ϵ_2 is also consistent with ϵ_a . Using the spectral evolution of a jet component, Lobanov & Zensus (1999) found evidence for a change from the synchrotron to the adiabatic stage at a distance of 1.2–1.5 mas from the core. This suggests that the transition from Compton to synchrotron stages is indeed observed. Future investigations on the spectral evolution of the jet are able to provide additional constraints on the transition regions between the Compton, synchrotron, and adiabatic stages.

3.2. Radio- γ -ray correlation

The correlation between radio and optical emission was studied in Schinzel et al. (2011) for identification of γ -ray emission from 3C 345. Here the connection between the synchrotron radio emission and γ -ray emission is investigated. To quantify a

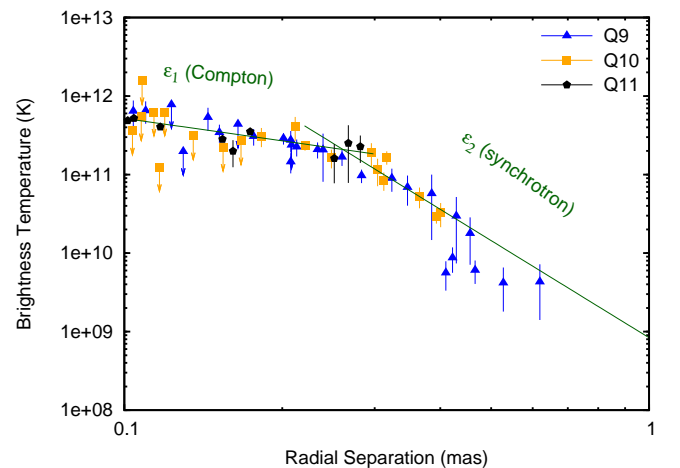


Fig. 4. Component brightness temperatures against radial separation from the VLBI core (Q0), representing the emission intensity gradient along the jet. Points with arrows are 1σ upper limits. Two lines are fitted to the data to determine the power law indices ϵ ($T_b \propto d_{\text{jet}}^{-\epsilon}$) from the data, the fit from 0.1 to 0.3 mas yields $\epsilon_1 = 0.95 \pm 0.69$ and 0.3 – 0.65 mas yields $\epsilon_2 = 4.11 \pm 0.85$.

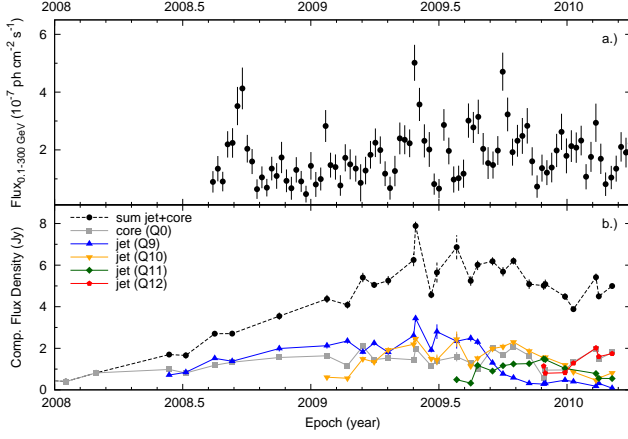


Fig. 5. *top:* Fermi LAT 7-day binned γ -ray light curve of 3C 345 for the energy range of 0.1–300 GeV. *bottom:* VLBA 7 mm component flux densities for the model-fitted VLBI core and inner jet, represented by up to five circular Gaussian (Q0, Q12, Q11, Q10, Q9). The component labeled Q0 is the east-most component (see Fig. 1) and represents the compact “core” or base of the jet. The black curve plots the sum of the flux densities of all four components.

possible connection, the correlation between the γ -ray and the radio light curve is calculated. For this we used the discrete correlation function presented by Edelson & Krolik (1988), which works well for unevenly sampled data. No statistically significant correlation is found, although around 2009.4, a rapid change in VLBI flux densities by ~ 1.5 Jy within only 4 days coincided well with a γ -ray flare (also see Fig. 5).

The top panel of Fig. 5 plots the weekly averaged γ -ray light curve of 3C 345. From it a seemingly long-term trend is seen, most evident between 2008.7 and 2009.4. After 2009.4 an increase in short-time variability is observed, followed by a slightly decreasing trend after 2009.8. The measured γ -ray flux increases by a factor of 2–3 between 2008.6 and 2009.5. Even more evident is a long-term trend in the light curve of the radio jet features (bottom panel of Fig. 5), following from the sum of the flux density of individual jet components. The optical R band data presented in Schinzel et al. (2011) similarly showed a rising trend for the same time period. This dataset is added for comparison as well.

To quantify this relation, the light curves are first rescaled with the zero flux representing their respective mean value. The radio flux density of the jet has a mean value of 3.60 Jy and corresponds to the emission from the jet of an apparent size of ≤ 2 pc (excluding the core). The core has a mean flux density of 1.5 Jy and an apparent size of ~ 0.3 pc. Note, the jet flux density is by a factor of 2.4 stronger than that of the core. The average γ -ray flux is $1.8 \cdot 10^{-7}$ ph cm $^{-2}$ s $^{-1}$. Observations at optical R band have an average magnitude of 16.6, which corresponds to a flux density of $7.7 \cdot 10^{-4}$ Jy.

In the final step, the rescaled light curves are de-trended using cubic spline interpolations over 0.4 year bins (Press et al. 1992). The extracted long-term trends are shown in Fig. 6. From these it is immediately evident that a similar trend is obtained for the radio jet and the γ -rays, whereas the core does not show a significant trend. The discrepancy of the first 0.4 year is caused by the lack of γ -ray monitoring before 2008.6 and a flare immediately after 2008.6 (see Fig. 5). The trend of the optical emission

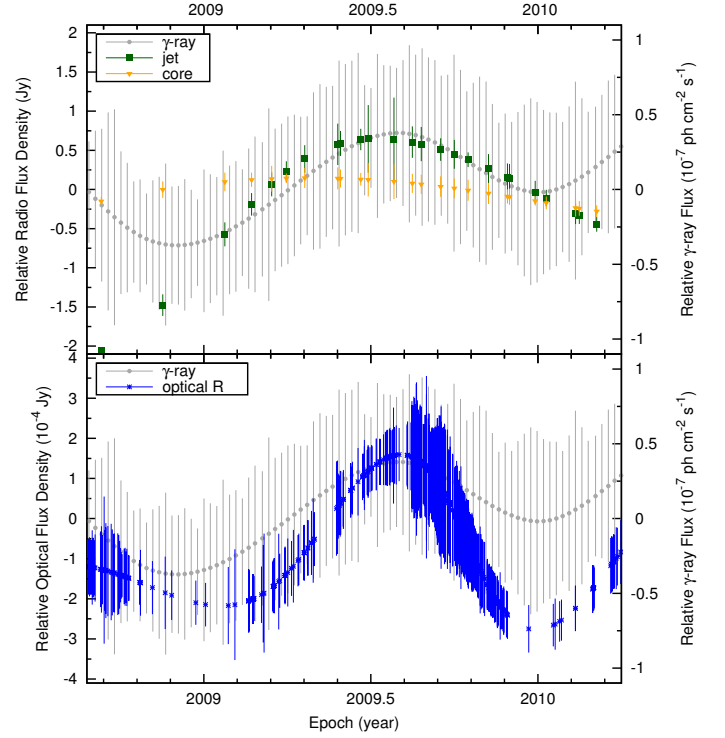


Fig. 6. Long-term trends of the radio jet, radio core flux densities, optical R band flux (Schinzel et al. 2010) and the γ -ray flux relative to their respective mean values (radio jet: 3.6 Jy, radio core: 1.5 Jy, optical R: 16.6^m ($7.7 \cdot 10^{-4}$ Jy), γ -ray: $1.8 \cdot 10^{-7}$ ph cm $^{-2}$ s $^{-1}$). The trend was extracted fitting cubic splines with 0.4 year bins. The relative radio flux density was scaled by a factor of 2:1 with respect to the relative γ -ray flux, the optical flux density was scaled by a factor of 4:1, and the data points match the sampling of the original light curves.

shows a similar behavior compared to the γ -ray and radio trends, however it is more peaked. Comparing trend amplitudes, the amplitude of the variation in the optical is 4 times greater than in the γ -rays. The radio shows a factor of 2 higher amplitude of the variation than γ -rays. Based on the peak values of these trends, the radio leads the γ -ray trend by 31^{+29}_{-11} days and optical leads the γ -ray trend by $1.1^{+11.3}_{-7.7}$ days. Altogether this is consistent with an almost zero time lag between the observed long-term trends.

The observed emission from the radio jet showing the matching trend is most of the time dominated by the jet component closest to the core. At the beginning of the monitoring period this is Q9 & Q10 and by the end of 2010 they are replaced by Q11 & Q12. This connects the emission from the radio jet with that observed at optical and γ -ray energies and places the site of the underlying multi-wavelength emission within the resolved 43 GHz radio jet. The very region that was shown to be Compton loss dominated in Section 3.1.3.

4. Discussion

Monitoring of the fine structure of the jet in 3C 345 reveals a wealth of morphological and kinematic features of the flow. In particular, compelling evidence for a stationary feature in the parsec-scale radio jet of 3C 345 is found. This stationary feature is located at a distance of ~ 0.1 mas (~ 0.7 pc) from the core. The kinematics of a large sample of relativistic jets, obtained

through the MOJAVE survey⁴, revealed stationary features as a frequent occurrence (Lister et al. 2009). In particular, in the jets of γ -ray blazars, observed at 22 and 43 GHz, stationary features within 2 pc (projected) from the core are commonly observed (Jorstad et al. 2001). Stationary jet features were investigated in more detail in the cases of 3C 390.3 (Arshakian et al. 2010), a nearby double-peaked radio galaxy at $z = 0.0561$, and the Seyfert galaxy 3C 120 ($z = 0.033$; León-Tavares et al. 2010). For these two sources, stationary features were found at distances of ~ 0.4 pc (3C 390.3) and ~ 1.3 pc (3C 120) from the core at 15 GHz. Their physical origin was associated with that of standing shocks. A more detailed investigation of the spectral evolution of a radio flare in CTA 102, a highly polarized quasar at $z=1.037$, provides supporting evidence for a shock-shock interaction scenario, providing a physical description for stationary features interacting with traveling shocks (Fromm et al. 2011).

The moving plasma condensations (components) are most likely generated near the base of the jet of 3C 345, but can only be reliably monitored after they pass through the location of the stationary feature. The nucleus of the jet lies at a distance of ~ 7 pc upstream from the 43 GHz VLBI core (Lobanov 1998b; Schinzel 2011). After the passage of the stationary feature, the superluminal components in 3C 345 undergo an apparent acceleration from ~ 5 to ~ 15 c over a distance of 0.3 mas in extent (~ 23 pc deprojected). This acceleration seems to be a commonly observed feature of many objects in the MOJAVE sample, where a statistically significant tendency for acceleration in the base of jets is found (Homan et al. 2009). Previously, Lobanov & Roland (2005) discussed the observed acceleration of a different component in 3C 345, testing the case of a substantially curved three-dimensional path, causing the observed dramatic change of the apparent component speed. They concluded that the observed acceleration is not likely to be a geometrical effect, but should reflect physical acceleration of plasma. The possibility of intrinsic acceleration of jet features on parsec scales was discussed by Vlahakis & Königl (2004). There it was specifically argued that the acceleration observed in 3C 345 is not purely hydrodynamic, but can be attributed to magnetic driving. They showed that the observed acceleration is consistent with an acceleration from $\Gamma \sim 5$ to $\Gamma \sim 10$ over a linear distance of ~ 3 to ~ 20 pc. The results presented here are consistent with these findings.

The times of passage of knots Q10, Q11, and Q12 through the 43 GHz VLBI core coincide with short-term increases in the γ -ray flux (see Fig. 5, with times listed in Table 2). In a similar case, PKS 1510-089 showed, in addition to the appearance of a new VLBI component, a rapid rotation in the optical linear polarization just prior the components passage through the core. This was explained by the feature following a spiral path through a toroidal field until it crosses a standing shock in the 43 GHz core (Marscher et al. 2010).

A γ -ray flare centered on 2009.4 may be related to the brightening of radio structure at distances of 0.12 – 0.20 mas from the core (0.8 – 1.3 pc), corresponding to a deprojected distance of ~ 9 –15 pc. Interestingly, this includes the region for which the presence of a standing shock is suggested by the observations presented in Sec. 3.1.1. Radio flares in the compact jet downstream of the VLBI core are known to occur (e.g., Wehrle et al. 2001). Furthermore, Jorstad et al. (2001, 2010) have found that γ -ray flares often occur after superluminal knots have separated from the VLBI core. The results presented here support the inference that γ -ray emission still occurs parsecs downstream

of the central engine, contrary to conclusions based on theoretical arguments (e.g., Tavecchio et al. 2010; Poutanen & Stern 2010). These arguments place the γ -ray emission zones within the broad-line region (BLR) at distances of $\lesssim 1$ pc from the central engine. Within this region a high number of optical–UV photons are produced (e.g. Kaspi et al. 2007), providing ideal conditions for inverse Compton scattering with relativistic electrons from the jet (e.g. Arshakian et al. 2011; Dermer et al. 1997). In addition, the observed variability time scales place constraints on the size of the emitting region due to causality arguments. Usually this size is related to the jet cross section, implying that the emission region is located close to the black hole. However, these standard assumptions do not necessarily need to be true.

In Section 3.2 we have shown that long-term trends observed at γ -ray and optical energies correlate with those of the radio emission at VLBI scales, which imply a common emission region. This emission region is related to the inner jet, extending over a distance of up to 23 pc from the VLBI core, which is at a distance of $\gg 1$ pc from the central engine, well beyond the BLR. The mechanism for the emission at radio and optical wavelengths is therefore dominated by the synchrotron emission from the relativistic jet itself. The simultaneity of γ -ray emission implies inverse Compton upscattering of synchrotron photons produced in the jet. The relative increase of optical and radio emission compared to γ -ray emission is a factor of 2 higher in the radio and even a factor of 4 higher in the optical emission, which is consistent with the mechanism of synchrotron self-Compton. An external contribution of “seed” photons, as proposed by external Compton scenarios (e.g. Tavecchio et al. 2010) is not required to produce the amount of the observed γ -ray emission. Additionally, we have found that the properties of the emission in this region are consistent with the Compton-loss stage of a shock (Section 3.1.3). Altogether, this contradicts the common theoretical high energy production scenario described in the previous paragraph. Recent observations of TeV emission from FSRQs (e.g. Aleksić et al. 2011) should not have been possible if the high energy emission site were within the BLR, which is expected to be opaque to γ -rays at TeV energies due to $\gamma\gamma$ interactions.

The observed kinematics of the jet is now combined with the rise times of the radio, optical, and γ -ray emission. The component Q9 is the first new component identified in 2008 and is most likely the emission region responsible for the initial flux increase. Using the long-term trends extracted, the distance at which Q9 was located during the onset of the flaring period in 2008 is ~ 0.05 mas from the VLBI core. This marks the region between the stationary feature and the core at 43 GHz. Instead of using the combined flux trend that is related to the sum of the radio emission regions, we calculate the time between the peak brightness of Q9 (2009.40) and the first γ -ray flare observed (2008.73). If we use the average component speed and assume no acceleration, then the closest Q9 could have been during the time of the first observed γ -ray flare is consistent with the position of the radio core at 43 GHz. This finding strongly supports the interpretation of the parsec-scale jet being responsible for driving the observed high energy emission.

Agudo et al. (2011) have reported on the location of a γ -ray flare in OJ 287, which was placed at a distance of more than 14 pc from the central engine. They proposed a model for the multi-wavelength emission where the high energy emission could be explained by the synchrotron self-Compton process or inverse Compton scattering of infrared radiation from a hot dusty torus, although it was concluded that the hot dusty torus scenario is less likely. In the case of 3C 345 it seems to be clear that mul-

⁴ <https://www.physics.purdue.edu/astro/mojave/>

multiple compact emission features are responsible for the observed variability and what seems to be a reasonable model for the case of OJ 287, could apply for 3C 345 as well. A new plasma disturbance passes through a first conical shock in the core and produces a fast rise in high energy emission; as it continues to propagate down the jet it continues to produce high energy emission.

5. Summary & Conclusions

Based on 32 VLBA observations of 3C 345 at 43.2 GHz, we have investigated the structure and evolution of the radio emission and related this to variations of the γ -ray and optical emission observed 2008–2010 by *Fermi*-LAT and a number of optical observatories.

We have identified and analyzed four new moving emission features (jet components) in the radio jet of 3C 345. These regions are found to move at apparent speeds of 9–15 c, with the corresponding Doppler and Lorentz factors derived to be in the ranges of 12–23 and 12–15, respectively. The kinematic data strongly favor a viewing angle of 4.7° between the jet axis and the line of sight.

We have presented evidence for the γ -ray emission to be produced not in a compact region near the central engine of the AGN, but in the Compton-loss dominated zone of the parsec-scale jet extending up to $r \approx 0.3$ mas, corresponding to a deprojected linear extent of ≈ 23 pc (accounting for the source distance and jet orientation). This zone is further marked by a break in the evolution of the brightness temperature, T_b , of the radio emission, with $T_b \propto r^{-(0.95 \pm 0.69)}$ at $r \leq 0.3$ mas and $T_b \propto r^{-(4.11 \pm 0.85)}$ at larger separations. Ejections of new superluminally moving and apparently accelerating features in the jet are linked to the flaring component of the γ -ray and optical emission.

These findings favor the synchrotron self-Compton mechanism of the high-energy emission production, while questioning the entire class of models that place the high energy emission site within 1 pc from the central engine of AGN, with external seed photons for inverse Compton scattering from the accretion disk or broad-line-region. They also imply that a significant part of the γ -ray emission is generated by highly-relativistic electrons propagating at a large bulk speed in the jet. In the context of newly emerging results, stimulated by *Fermi* data, more detailed analytical and numerical descriptions of such a scenario are clearly needed in order to explain the observed connection between radio and γ -ray variability. At the same time, continued monitoring and more densely sampled VLBI observations of well studied, bright blazar radio jets represent an essential requirement for improving the degree of detail and statistical accuracy of the correlation reported and further improving the spatial localization of individual flares in relativistic jets.

Acknowledgements. We thank Nicola Marchili for providing us with his implementation of the cubic spline de-trending algorithm. We thank the anonymous referee for valuable comments. Frank Schinzel was supported for this research through a stipend from the International Max-Planck Research School (IMPRS) for Astronomy and Astrophysics at the Universities of Bonn and Cologne. We thank NASA for support under FERMI grant GSFC #21078/FERMI08-0051. The research at Boston University was supported in part by NASA through *Fermi* Guest Investigator grants NNX08AJ64G, NNX08AU02G, NNX08AV61G, and NNX08AV65G, and by National Science Foundation grant AST-0907893. The National Radio Astronomy Observatory is a facility of the National Science Foundation operated under cooperative agreement by Associated Universities, Inc. This research has made use of the NASA/IPAC Extragalactic Database (NED) which is operated by the Jet Propulsion Laboratory, California Institute of Technology, under contract with the National Aeronautics and Space Administration. This research has made use of NASA's Astrophysics Data System.

References

- Abdo, A. A., Ackermann, M., Ajello, M., et al. 2010, *ApJS*, 188, 405
 Abdo, A. A., Ackermann, M., Ajello, M., et al. 2009, *ApJ*, 700, 597
 Agudo, I., Jorstad, S. G., Marscher, A. P., et al. 2011, *ApJ*, 726, L13
 Aleksić, J., Antonelli, L. A., Antonarz, P., et al. 2011, *ApJ*, 730, L8
 Aller, H. D., Aller, M. F., & Hughes, P. A. 1996, in *Astronomical Society of the Pacific Conference Series*, Vol. 110, *Blazar Continuum Variability*, ed. H. R. Miller, J. R. Webb, & J. C. Noble, 208
 Arshakian, T. G., León-Tavares, J., Boettcher, M., et al. 2011, eprint arXiv:1104.4946
 Arshakian, T. G., León-Tavares, J., Lobanov, A. P., et al. 2010, *MNRAS*, 401, 1231
 Atwood, W. B., Abdo, A. A., Ackermann, M., et al. 2009, *ApJ*, 697, 1071
 Avni, Y. 1976, *ApJ*, 210, 642
 Baath, L. B., Rogers, A. E. E., Inoue, M., et al. 1992, *A&A*, 257, 31
 Babadzanyants, M. K. & Belokon, E. T. 1984, *Astrophysics*, 20, 461
 Biretta, J. A., Moore, R. L., & Cohen, M. H. 1986, *ApJ*, 308, 93
 Błażejowski, M., Siemiginowska, A., Sikora, M., Moderski, R., & Bechtold, J. 2004, *ApJ*, 600, L27
 Böttcher, M., Reimer, A., & Marscher, A. P. 2009, *ApJ*, 703, 1168
 Casandjian, J.-M. & Grenier, I. A. 2008, *A&A*, 489, 849
 Dermer, C. D., Finke, J. D., Krug, H., & Böttcher, M. 2009, *ApJ*, 692, 32
 Dermer, C. D., Sturmer, S. J., & Schlickeiser, R. 1997, *ApJS*, 109, 103
 Edelson, R. A. & Krolik, J. H. 1988, *ApJ*, 333, 646
 Fomalont, E. B. 1999, in *Astronomical Society of the Pacific Conference Series*, Vol. 180, *Synthesis Imaging in Radio Astronomy II*, ed. G. B. Taylor, C. L. Carilli, & R. A. Perley, 301
 Fromm, C. M., Perucho, M., Ros, E., et al. 2011, *A&A*, 531, A95+
 Hirotani, K. 2005, *ApJ*, 619, 73
 Homan, D. C., Kadler, M., Kellermann, K. I., et al. 2009, *ApJ*, 706, 1253
 Jorstad, S. G., Marscher, A. P., Lister, M. L., et al. 2005, *AJ*, 130, 1418
 Jorstad, S. G., Marscher, A. P., Mattox, J. R., et al. 2001, *ApJS*, 134, 181
 Jorstad, S. G., Marscher, A. P., Smith, P. A., Larionov, V. M., & I., A. 2010, in *Fermi meets Jandky - AGN in Radio and Gamma Rays*, ed. T. Savolainen
 Jorstad, S. G., Marscher, A. P., Stevens, J. A., et al. 2007, *AJ*, 134, 799
 Kaspi, S., Brandt, W. N., Maoz, D., et al. 2007, *ApJ*, 659, 997
 Kidger, M. & Takalo, L. 1990, *A&A*, 239, L9
 Klare, J. 2004, PhD thesis, Rheinische Friedrich-Wilhelms-Universität Bonn, Bonn, Germany, (2004)
 Larionov, V. M., Villata, M., Raiteri, C. M., et al. 2009, *The Astronomer's Telegram*, 2222, 1
 León-Tavares, J., Lobanov, A. P., Chavushyan, V. H., et al. 2010, *ApJ*, 715, 355
 Lister, M. L., Cohen, M. H., Homan, D. C., et al. 2009, *AJ*, 138, 1874
 Lobanov, A. P. 1996, PhD thesis, New Mexico Institute of Mining & Technology, Socorro, NM, US, (1996)
 Lobanov, A. P. 1998a, *A&AS*, 132, 261
 Lobanov, A. P. 1998b, *A&A*, 330, 79
 Lobanov, A. P. 2005, eprint arXiv:astro-ph/0503225
 Lobanov, A. P. & Roland, J. 2005, *A&A*, 431, 831
 Lobanov, A. P. & Zensus, J. A. 1999, *ApJ*, 521, 509
 Longair, S. M. 2011, *High Energy Astrophysics* (Cambridge University Press)
 Marscher, A. P. & Gear, W. K. 1985, *ApJ*, 298, 114
 Marscher, A. P., Gear, W. K., & Travis, J. P. 1992, in *Variability of Blazars*, ed. E. Valtaoja & M. Valtonen, 85
 Marscher, A. P., Jorstad, S. G., Larionov, V. M., et al. 2010, *ApJ*, 710, L126
 Marziani, P., Sulentic, J. W., Dultzin-Hacyan, D., Calvani, M., & Moles, M. 1996, *ApJS*, 104, 37
 Pearson, T. J. 1999, in *Astronomical Society of the Pacific Conference Series*, Vol. 180, *Synthesis Imaging in Radio Astronomy II*, ed. G. B. Taylor, C. L. Carilli, & R. A. Perley, 335
 Poutanen, J. & Stern, B. 2010, *ApJ*, 717, L118
 Press, W. H., Teukolsky, S. A., Vetterling, W. T., & Flannery, B. P. 1992, *Numerical recipes in FORTRAN. The art of scientific computing*, ed. Press, W. H., Teukolsky, S. A., Vetterling, W. T., & Flannery, B. P.
 Pushkarev, A. B., Kovalev, Y. Y., Lister, M. L., & Savolainen, T. 2009, *A&A*, 507, L33
 Ros, E., Zensus, J. A., & Lobanov, A. P. 2000, *A&A*, 354, 55
 Schinzel, F. K. 2011, PhD thesis, University of Cologne
 Schinzel, F. K., et al., & for the *Fermi*-LAT collaboration. 2011, *A&A*, accepted, to appear in preprints and on astro-ph
 Shepherd, M. C., Pearson, T. J., & Taylor, G. B. 1995, in *Bulletin of the American Astronomical Society*, Vol. 27, *Bulletin of the American Astronomical Society*, ed. B. J. Butler & D. O. Muhleman, 903
 Tavecchio, F., Ghisellini, G., Bonnoli, G., & Ghirlanda, G. 2010, *MNRAS*, 405, L94
 Teraesranta, H., Tornikoski, M., Mujunen, A., et al. 1998, *A&AS*, 132, 305
 Thompson, D. J., Bertsch, D. L., Fichtel, C. E., et al. 1993, *ApJS*, 86, 629

- Unwin, S. C., Wehrle, A. E., Lobanov, A. P., et al. 1997, *ApJ*, 480, 596
Valtaoja, E. & Teraesranta, H. 1996, *A&AS*, 120, C491
Vlahakis, N. & Königl, A. 2004, *ApJ*, 605, 656
Wehrle, A. E., Piner, B. G., Unwin, S. C., et al. 2001, *ApJS*, 133, 297
Zensus, J. A., Cohen, M. H., & Unwin, S. C. 1995, *ApJ*, 443, 35